Biophysical Journal, Volume *117*

Supplemental Information

The Roles of Microtubules and Membrane Tension in Axonal Beading, Retraction, and Atrophy

Anagha Datar, Jaishabanu Ameeramja, Alka Bhat, Roli Srivastava, Ashish Mishra, Roberto Bernal, Jacques Prost, Andrew Callan-Jones, and Pramod A. Pullarkat

Supporting Material

Quantification of inter-bead distance and its dependence on initial radius:

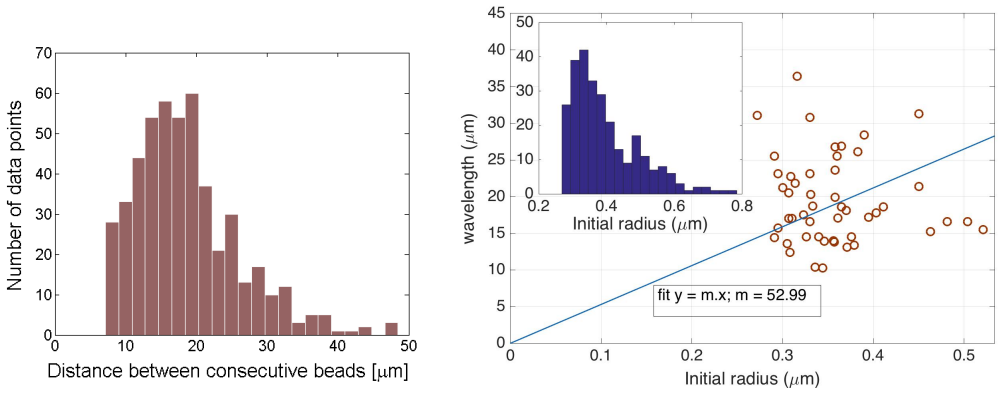

Fig. S1: Characterization of beading as a result of 15 ± 3 min. exposure to 16.7 μM nocodazole. **Left:** distribution of distance between consecutive beads (n = 490 bead pairs). **Right:** plot of averaged distance between beads per axon (wavelength) versus the averaged initial radius of an axon (n = 50 axons). The fitted line was forced through the origin. This linear fit is motivated by the expected scaling of the most unstable beading wavelength with the initial radius of the axon, as predicted by Rayleigh-Plateau type instabilities (1). The inset shows the distribution of initial radius (n = 272).

Local application of nocodazole using dual micropipettes:

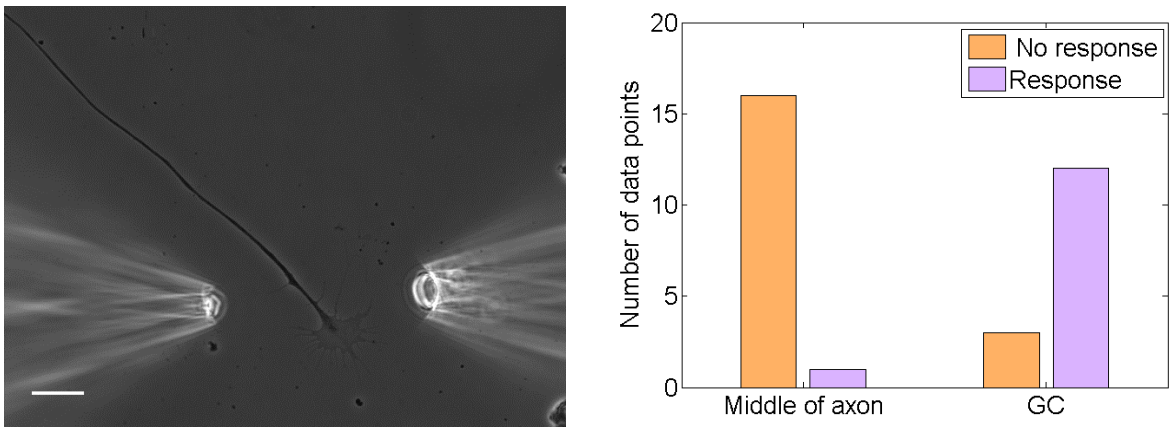

Fig. S2: Left: Dual micropipette arrangement for local application of Noco at the growth cone (GC) of an axon, using an infusion pipette on left and a suction pipette on right (bar: 20μm). The infusion and suction are controlled using XenoWorks Digital Microinjector (Sutter Instruments Co.). The typical concentration profile around the application point was measured using a fluorescent dye instead of Noco. The drug exposure was restricted to about 10 μm of the axon shaft. **Right:** quantification of the beading response of axons to such local treatment using 33 μM Noco, depending upon the location of drug application. Distal shaft next to the growth cone is seen to be much more vulnerable than the proximal shaft.

Membrane tension measurements:

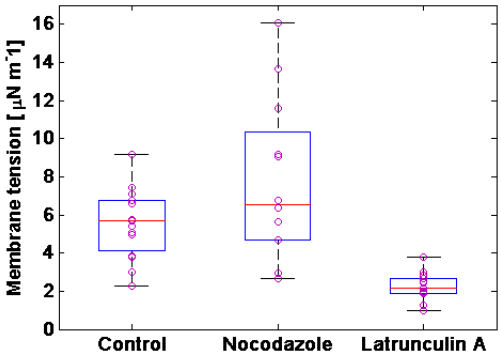

Fig. S3: Membrane tension measured using steady state membrane tethers extracted out of axons using an optical tweezers (see Datar et al., Biophysical Journal, vol. 108, pages 489-497, year 2015 for details) . Data for control cells, cells treated with 16.67 μM Nocodazole and cells treated with 1 μM Latrunculin-A are shown (n = 12 axons each). The horizontal red lines are the medians and the boxes are bound by the 25th and 75th percentiles in each case. The whiskers mark the extreme data points.

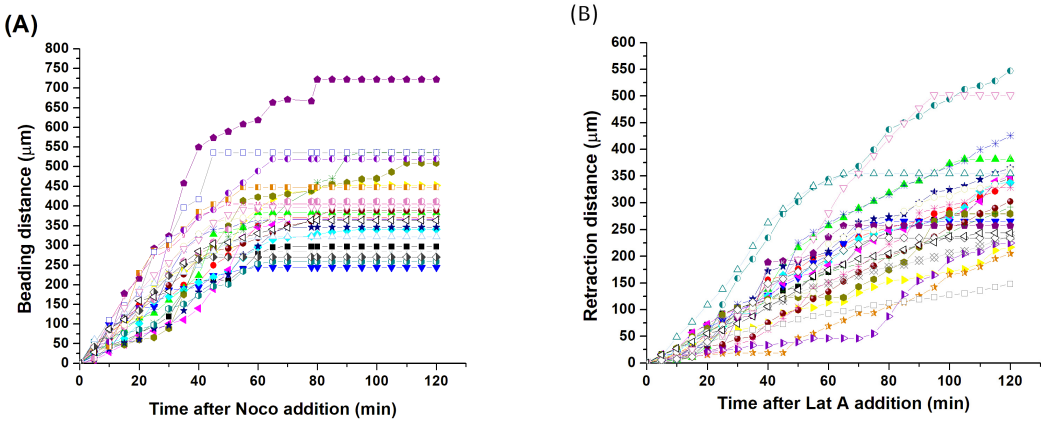

Fig. S4: **(A)** Data for individual axons showing how the distance over which beading is observed grows with time. The distances corresponding to the last time point gives the length of the respective axon. Distances are measured from the growthcone. **(B)** Data for individual axons showing how the distance over which retraction has progressed grows with time. The distances corresponding to the last time point gives the length of the respective axon. The averaged data for both cases are shown in the main text.

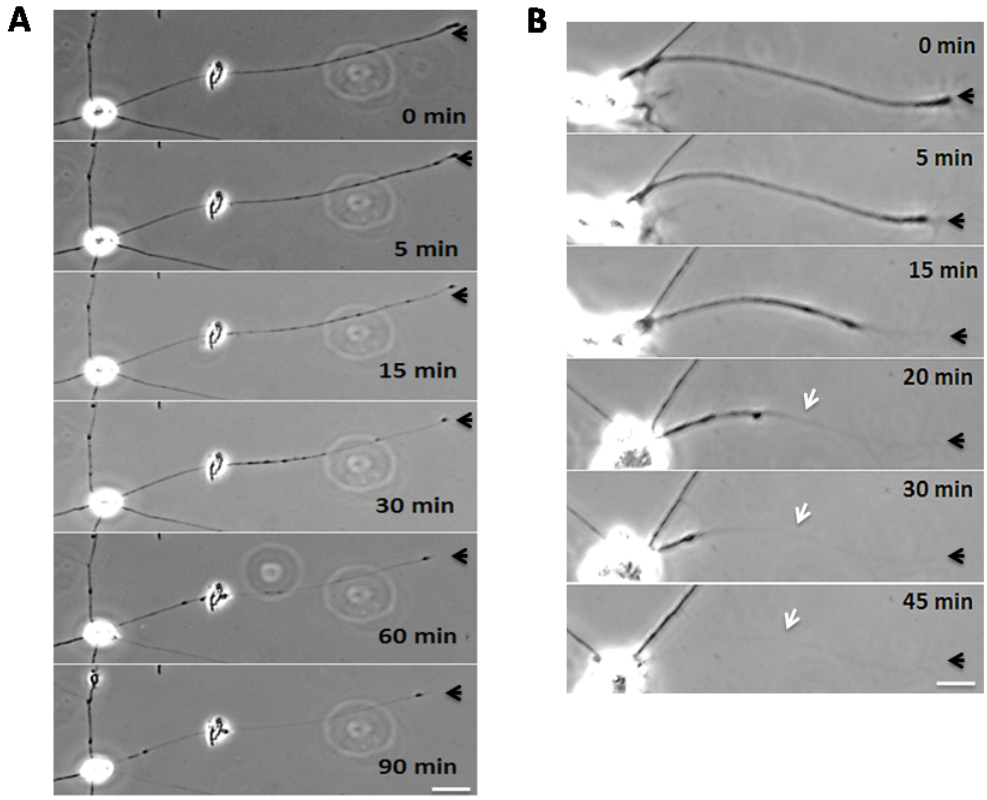

Fig. S5: (A) Image sequence showing beading of axons treated with high concentration (10 µM) Latrunculin-A. Black arroheads show the location of the growth cone. **(B)** Image sequence showing an example of retraction happening under the influence of low concentration (3.33 µM) Nocodazole. Scale bars are 10 µm.

Laser ablation:

We observed that the immediate response of axons to laser ablation is of a very fast retraction away from the point of cut (**Fig. S6-A**). We call it snapping. To test whether this is a mechanical response of the axon or just a laser induced damage, we performed the same experiment using cells fixed with glutaraldehyde. These cells did not show any significant snapping (**Fig. S6-B**). Subsequent to the sudden shortening, untreated axons show buckling and/or beading and in some cases, folding back of the cut tips away from the point of laser ablation. Beading appears to progress away from the point of laser ablation (**Movies S8,S9**).

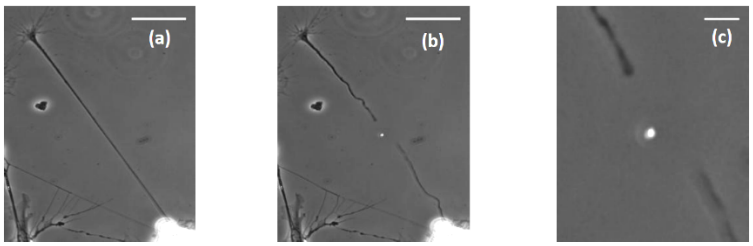

Fig. S6-A: An axon before **(a)** and after **(b)** a laser cut (bar: 40 µm). Magnified part of image (b) is shown in **(c)** (bar: 8 µm). After the cut, axons under go a sudden retraction which accompanied by buckling and then a slower retraction.

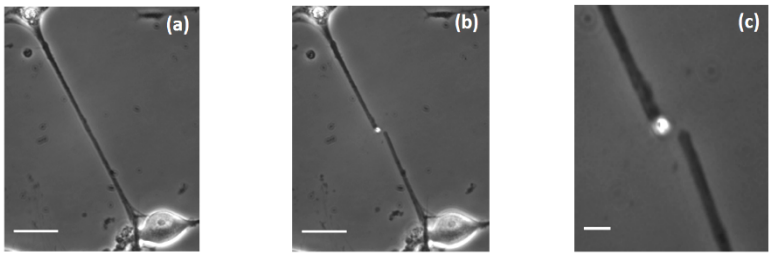

Fig. S6-B: A glutaraldehyde-fixed axon before **(a)** and after undergoing laser cut **(b)** (bar: 40 µm). Magnified part of image (b) is shown in **(c)** (bar: 8 µm). Fixed axons do not show any significant shortening after the cut. This shows that the laser cut itself is clean and shortening in non-fixed cells is a true axonal response to transection.

Distribution of snapping distance after laser transection of axons:

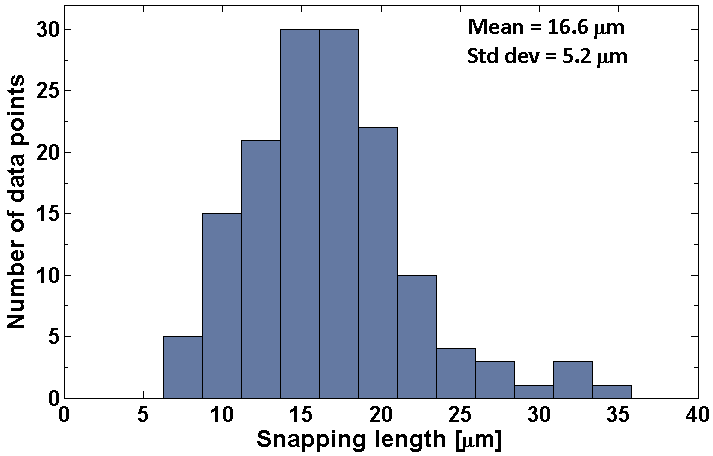

Fig. S7: Distribution of snapping distance after laser transection of 72 axons, with mean 16.6 µm and standard deviation 5.2 µm. The snapping and buckling responses (see **Fig. S6-A**) show that the axons are under significant rest tension.

Beading observed in PC12 neurites treated with either Latrunculin-A or Nocodazole:

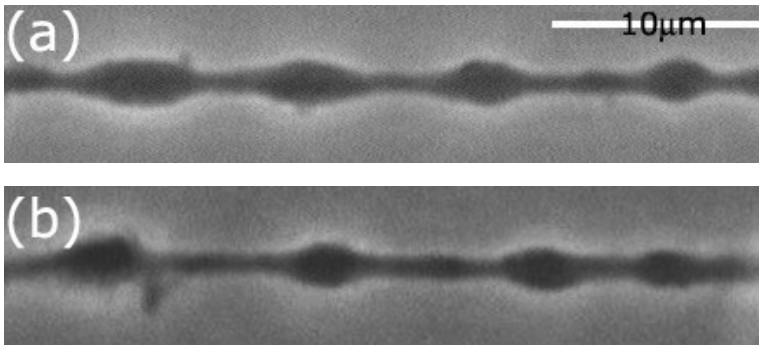

(c)

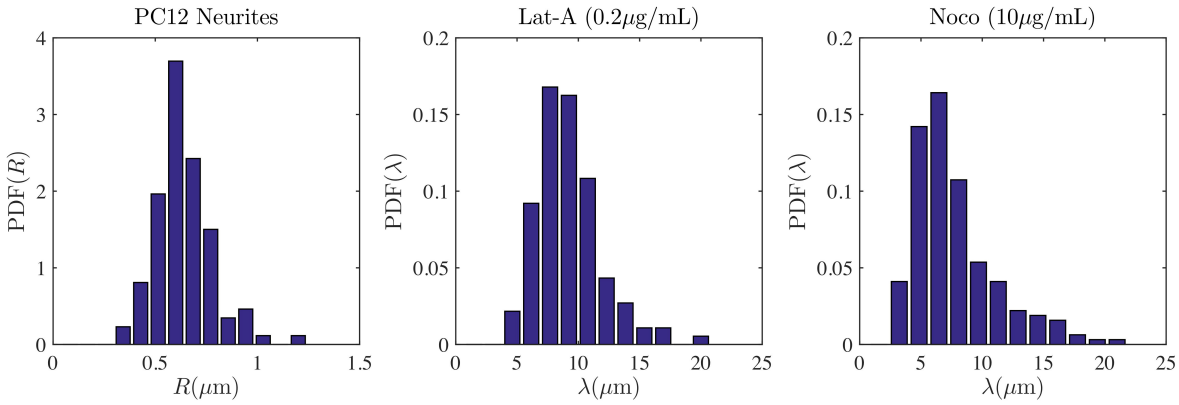

(d)

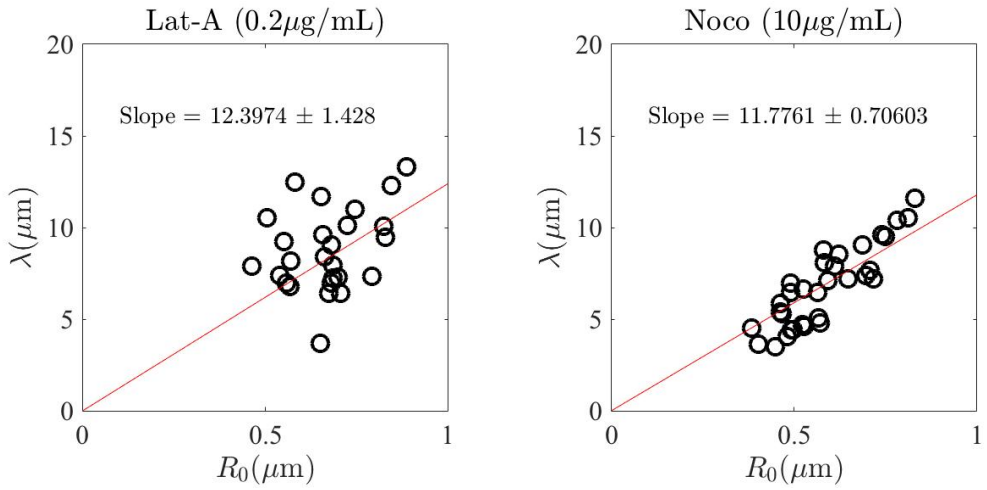

Fig. S8: Neurites of mouse PC12 cells show beading when either microtubules or f-actin is pharmacologically disrupted. **(a)** Beading observed in PC12 cells when treated with 10 μg/ml Nocodazole (Noco). **(b)** Beading in PC12 cells occurring as a result of exposure to 0.2 μg/ml Latrunculin-A (Lat-A). **(c)** The distributions of the initial radius and the beading wavelengths for PC12 cells treated with either Noco or Lat-A as indicated on the plots. **(d)** Wavelength (λ) vs initial radius (R_0) plots for PC12 cells treated with Noco or Lat-A as indicated above the figures. The fits are forced through (0,0). R-squared values are -0.272 for Lat-A and 0.694 for Noco.

Analysis of bead shape:

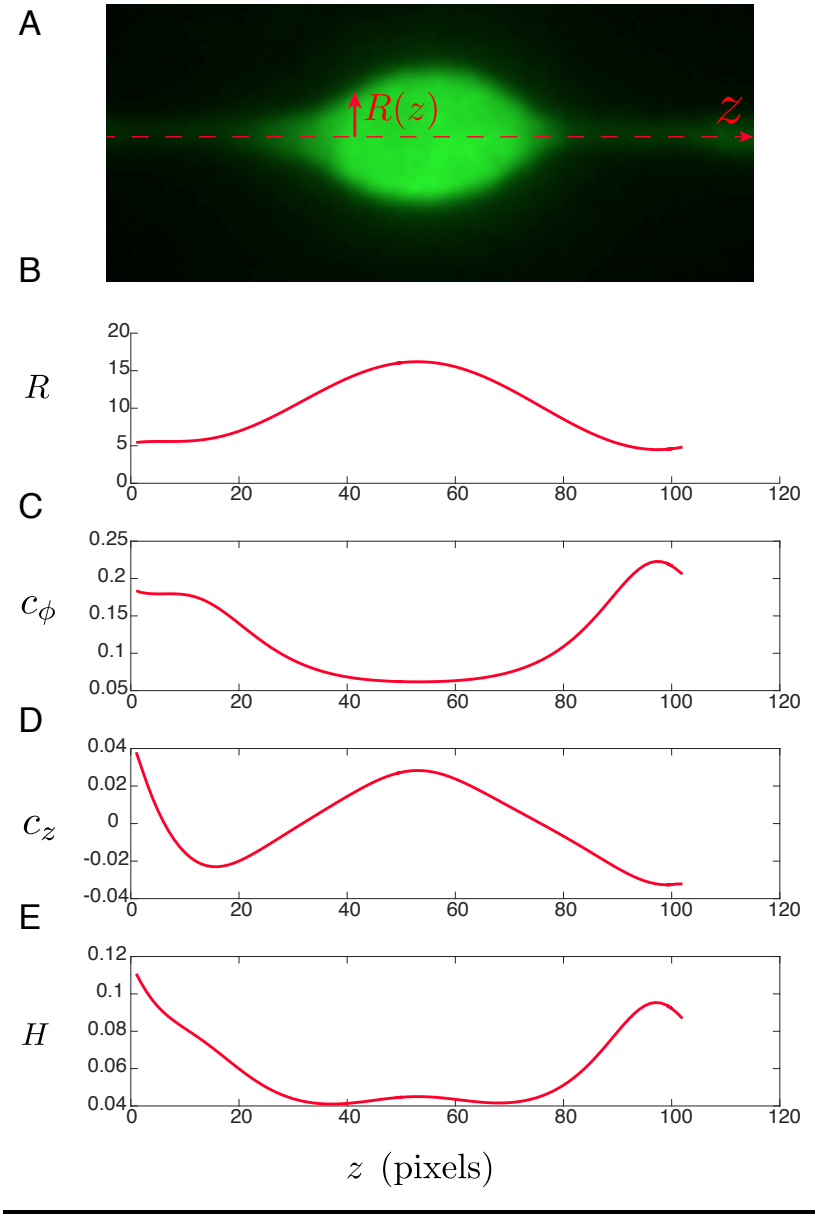

Fig. S9: Analysis of bead shapes reveals balance of forces on axon surface. **(A)** Fluorescence image of axon bead after Noco treatment. **(B)** Radial distance from centerline to axon bead surface, R, as a function of axial position, z. R is in pixels. **(C)** Principal curvature of bead surface in plane perpendicular to R and z, as a function of z. **(D)** Principal curvature of bead surface in (R, z) plane, as a function of z. **(E)** Mean curvature of surface, H, as a function of z. Curvatures are expressed in inverse pixels.

Table S1 :

Noco beading

Drug	No of beaded axons	Total no of axons
Nocodazole	121	126
Y-27632 + Nocodazole	123	143

Lat-A retraction

Drug	No of retracted axons	Total no of axons
Latrunculin A	137	141
Y-27632 + Latrunculin A	149	151

Table S1: Quantification of beading or retraction events after pre-treating cells with the 30 μM Rho Kinase inhibitor Y-27632 for 20 min in each case. The quantification was done after 20 min of exposure to Noco at 16.6 μM or Lat-A at 1 μM.

Table S2 :

Quantification of beading and retraction as a function of drug concentration:

Drug	Concentration	Beading (%)	Retraction (%)	No. of axons
Nocodazole	3. 33 μM	71.26	12.64	90
Nocodazole	33.3 μM	95.2	4.81	104
Latrunculin A	1 μM	3	97	100
Latrunculin A	10 μM	18.75	81.25	75
Blebbistatin	30 μM	0	0	17

Table S2. Quantification of the concentration dependence of percentage of beading and retraction upon different drug treatments. Note that while Nocodazole predominantly causes beading, some percentage of retraction is also observed, and this number is higher at lower Noco concentration. And in the case of Latrunculin-A, the predominant mode is retraction, but an increasing percentage of beading close to the retracting front is observed with increasing Lat-A concentration. Blebbistatin treatment alone did not cause any beading or retraction (> 30 min wait time).

Appendix S1

Rayleigh-Plateau and Pearling instabilities:

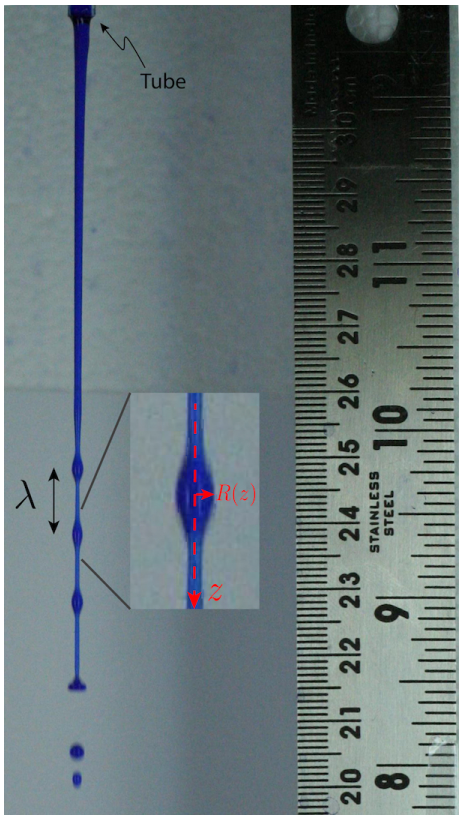

A cylindrical column of any fluid is unstable and will break up into a series of droplets. This break-up is driven by surface tension σ. This is because there is a net reduction in surface area in going from a cylinder of radius R_0 to a series of n spherical drops of radius R_s of same net volume. Since the total volume has to be conserved, this gives a cylinder-to-spherical drops surface area ratio $\frac{A_c}{nA_s} = \frac{3R_0}{2R_s}$. Thus, a series of spheres with $R_s > \frac{3}{2} R_0$ has a lower surface area compared to the original cylinder. As a result, a fluid cylinder is unstable to shape perturbations with wavelengths greater than R_0.

This is, of course, a static argument, and the actual shape change of the fluid cylinder depends on dynamics. It was shown by Rayleigh that the shape evolution happens via sinusoidal peristaltic modes. Sinusoidal perturbation of the radius of the form $R(z) = R_0 + \varepsilon \sin(2\pi z/\lambda)$ reduces surface area provided the wavelength $\lambda > 2\pi R_0$ (ignoring epsilon square terms which guaranty constant volume). In such cases, the higher Laplace pressure ($P \sim \sigma/R$) in the thinner parts drive fluid to the thicker parts leading to the fomation of a series of bulges that grow with time until break-up. The optimal wavelength—the fastest growing mode—is decided by a competition between the gain in surface energy for a given wavelength and the time scale for fluid transfer. Long wavelengths (resulting in fewer final drops) are energetically more favourable but they are slow to grow as they require transport of fluid over long distances (trough to crest). Short wavelengths require fluid flow over short distances but also results in less energy gain and hence slow to grow. Thus, in experiments only the fastest growing mode becomes apparent.

An easy way to obtain a fluid cylinder is to allow fluid to fall free from a vertical faucet. The image on the left shows a snapshot of ink coloured water dropping from a plastic tube which can be seen at the top. The vertical axis can be thought of as time with zero time at the tube opening.

The mechanism is similar for a synthetic lipid bilayer membrane tubes filled with a fluid undergoing "Pearling instability", expect that in this case the tube is unstable only if the membrane is under tension (an unconstrained piece of lipid bilayer has zero tension and hence zero interfacial elastic free energy). Moreover, the gain in surface energy has to overcome the cost of bending the membrane. Hence there is a small but finite critical tension for the tube to become unstable to Rayleigh-Plateau-like modes (2).

If the membrane tube is filled with an elastic matrix, like in the case of axons, there is a bulk elastic free enrgy cost for shape change as any deformation increases the free energy. This increases the threshold tension required for beading. In a highly simplified case, this critical tension goes as $\sigma_c \sim ER_0$, where E is the bulk elastic shear modulus (1). If E is reduced due to "melting" of the bulk material, the tube can develop peristaltic modes under very low membrane tension. In axons, depolymerization of microtubules generate a fluid-like layer between the stable core and the outer membrane which makes the membrane unstable to beading-like modes. If the core has a thickness gradient, the beads will propagate as in the case of conical wires wetted by a viscous fluid (3). In axons, the instability can be very periodic when the driving force is strong (high membrane tension) as in osmotic-shock

experiments (here only axons which were not attached to the substrate were used). When driving is weak (low membrane tension as in Noco. experiments), structural heterogeneities and adhesive contacts with the growth substrate cause significant dispersion in bead distribution (**Fig. S1**).

Appendix S2

Bead shapes at long times after Noco treatment

To further test the capillary (i.e., membrane tension) origin of Noco-induced beading, we analyzed the shape of an isolated bead at long times after treatment; see **Fig. S9A**. **Figure 2** in main the article shows a remaining microtubule track long after Noco treatment is applied, suggesting a resemblance between axon beading and Rayleigh-Plateau instability-driven dewetting of a liquid film on a cylindrical fiber. In this case, it is well known that the instability saturates to a final pattern of static, isolated droplets. The shape of these droplets can be derived from Laplace's law: $H = P/(2\sigma)$, where H is the surface mean curvature, P is the fluid pressure and σ the liquid-vapor interfacial tension. At equilibrium P is uniform, and therefore H is, as well. From this, the shape of axisymmetric droplets on the fiber can be obtained (4).

To see whether axons can be analyzed in a similar manner, we first mathematically characterized the surface of a typical axon bead by determining the radial distance, $R(z)$, from the bead centerline to the bead contour in the image plane as a function of distance along the axon, z; see **Fig. S9A**. Then, by fitting the contour data (**Fig. S9A**) and assuming that the bead is axisymmetric, we calculated the surface principal curvature in the orthoradial direction, $c_\phi = \frac{1}{R(z)\sqrt{1+(dR/dz)^2}}$ (**Fig. S9B**); the principal curvature in the (R, z) plane, $c_z = -\frac{d^2R/dz^2}{\sqrt{[1+(dR/dz)^2]^3}}$ (**Fig. S9C**); and the mean curvature $H = (c_\phi + c_z)/2$, (**Fig. S9D**). Interestingly, there is a central region of the bead where H is approximately constant, suggesting that the bead is liquid and with a surface shape governed by a competition between internal pressure and membrane tension. However, the mean curvature increases by roughly a factor of two near the bead edges, where the axon surface is expected to interact with the remaining microtubule core, a behavior which does not occur for liquid droplets wetting a fibre.

We argue that this difference is likely due to the bending rigidity, κ, of the membrane enclosing the axon. That is, the shape of the axon surface, $R(z)$, is determined by a balance of forces *and* torques acting on each surface element; in contrast, the shape of a liquid droplet only involves forces. This translates into requiring greater specification of boundary conditions along the contact line (CL) between the surface and the central fibre than in the liquid case. Namely, H is *imposed* along the CL, and is likely quite different than the value given by $P/(2\sigma)$. We therefore expect there to be a region of thickness of order $\ell = \sqrt{\kappa/\sigma}$ (the characteristic length scale of the membrane), over which H varies from the boundary value to the bulk value $P/(2\sigma)$. At distances away from the bead edges large compared with ℓ, bending becomes irrelevant and the bead shape is controlled by pressure and tension. Taking $\kappa = 3 \times 10^{-19}$ J, as measured for chicken DRG neuronal membrane (5), and $\sigma = 8 \times 10^{-6}$ N/m obtained for our Noco-treated axons, we find $\ell \approx 200$ nm. Note that this value could be modified by the rigidity conferred by the actin-spectrin skeleton. Thus, at long times after axon beading begins, the deformed shape can be understood as arising from a simple balance of forces and torques involving uniform pressure, surface tension, and bending rigidity.

Supporting References:

1) Pullarkat, P.A., P. Dommersnes, P. Fernández, J.F. Joanny, and A. Ott. 2006. Osmotically driven shape transformations in axons. Phys. Rev. Lett. 96: 1–4.
2) Bar-Ziv, R., and E. Moses. 1994. Instability and "pearling" states produced in tubular membranes by competition of curvature and tension. Phys. Rev. Lett. 73: 1392–1395.
3) Lorenceau, E., and D. Quéré. 2004. Drops on a conical wire. J. Fluid Mech. 510: 29–45.
4) Carroll, B.J. 1976. The accurate measurement of contact angle, phase contact areas, drop volume, and Laplace excess pressure in drop-on-fiber systems. J. Colloid Interface Sci. 57: 488–495.
5) Hochmuth, R.M., Shao, J.Y., Dai, J., and Sheetz, M.P. 1996. Deformation and flow of membrane into tethers extracted from neuronal growth cones. Biophys. J., 70: 358—369.

Captions for Movie files S1 to S11:

Movie S1: Time lapse recording of two axons with their growth cones located towards the bottom of the field of view (FoV). The recording started 1 min after Noco was added to the dish. The onset of beading can be seen around 2 min 24 s for both the axons, starting at their respective growth cone ends. Beading progresses with coarsening and retrograde migration (t ~ 20 min onwards). At 31 min 42 s the FoV is changed to the location of the soma. Time is shown in min:sec.

Movie S2: Time lapse recording of an axon with the soma on right as indicated by the arrow in the first frame. The recording was started at 35 min after Noco was added to the dish. Thus, beading can be seen already in the beginning of the movie. A clear retrograde migration of the beads can be seen throughout the movie, leaving behind a thin membrane trail. Time is shown in min:sec, and the scale bar is 10 micron.

Movie S3: Phase contrast imaging of transport in an axon as it undergoes beading. The recording was started 5 min after adding 16.6 μM of Noco. Images were recorded using an 100X objective and the image histogram was adjusted by setting a minimum and maximum cutoffs to highlihgth the dense particles. Time in hr:min:sec.

Movie S4: Time lapse recording of the movement of GFP-synaptophysin tagged synaptic vesicles in a control axon. Time is in hr:min:sec:m-sec, and the scale bar is 10 microns.

Movie S5: Time lapse recording of the movement of GFP-synaptophysin tagged synaptic vesicles in a Noco treated axon. Beading progresses during the course of the movie. Time is in hr:min:sec, and the scale bar is 10 microns.

Movie S6: Time lapse recording of a Lat-A treated axon with a healthy growth cone visible in the beginning. In the first few frames the growth cone deforms and shrinks. Later the contents begin to retract leaving behind a much thinner trail of membrane. In another vertically oriented axon in the same movie, the retraction front can be very clearly seen from 16 min onwards. The time is shown in hr:min:sec, and the scale bar is 10 microns.

Movie S7: Time lapse recording showing an axon which was pretreated with Taxol and then with Lat-A. The recording was started soon after adding Lat-A. The growth cone begin to collapse as soon as Lat-A is added but no further retraction is observed. Time is in hr:min:sec.

Movie S8: Time lapse recording of laser ablation and ensuing retraction of an axon. The appearance of a bright spot indicate the point where the laser pulse has hit. The bright spot persists because the laser had caused micro-cracks on the upper surface of the coverslip resulting in scattering of light. Note that the axon is not completely transected. There is a very thin tube of membrane connecting the two thicker

segments on both sides. Until the thin connection between the two retracting segments is intact, the two retracting segments lie along a line. In cases where the cut is complete, the axon snaps back suddenly and also buckles (see **Fig. S6a**). Time is shown in min:sec.

Movie S9: Time lapse recording of laser ablation of an axon which exhibit beading in the retracting segments. The axon has not been completely transected and the retracting segments are connected by a thin tube. Time is shown in min:sec

Movie S10: Time lapse recording of a PC12 neurite undergoing pearling instability when subjected to an osmotic shock. The thickness of the axon is about a micron and the duration of the video is about 1 min. Time is in min:sec.

Movie S11: Time lapse recording of a PC12 neurite treated with 10 micro-gram/ml Noco. Time is in hr:min:sec.

****